Eur. Phys. J. E **27**, 123–133 (2008)
DOI 10.1140/epje/i2008-10358-7

THE EUROPEAN PHYSICAL JOURNAL E

Numerical modelling of foam Couette flows

I. Cheddadi[1], P. Saramito[1,a], C. Raufaste[2,b], P. Marmottant[2], and F. Graner[2]

[1] Laboratoire Jean Kuntzmann, Université J. Fourier, CNRS and INRIA, 51, rue des Mathématiques, 38400 Saint-Martin d'Hères Cedex, France
[2] Laboratoire Spectrométrie Physique, UMR 5588, CNRS and Université J. Fourier, B.P. 87, 38402 Saint-Martin d'Hères Cedex, France

Received 6 February 2008 and Received in final form 28 April 2008
Published online: 11 September 2008 –

Abstract. A numerical computation based on a tensorial visco-elasto-plastic model based on continuous mechanics is compared to experimental measurements on liquid foams for a bidimensional Couette flow between two glass plates, both in stationary and transient cases. The main features of the model are elasticity up to a plastic yield stress, and viscoelasticity above it. The effect of the friction of the plates is taken into account. The numerical modelling is based on a small set of standard material parameters that are fully characterised. Shear localisation as well as acute transient observations are reproduced and agree with experimental measurements. The plasticity appears to be the fundamental mechanism of the localisation of the flow. Finally, the present approach could be extended from liquid foams to similar materials such as emulsions, colloids or wet granular materials, that exhibit localisation.

PACS. 47.57.Bc Foams and emulsions – 83.60.La Viscoplasticity; yield stress – 83.60.Df Nonlinear viscoelasticity – 02.60.Cb Numerical simulation; solution of equations

Introduction

The bidimensional Couette flow of a foam has been widely studied, from experimental, theoretical and numerical points of view. Many studies focus on the velocity profile that can localise near the moving walls [1,2]: the measurements exhibit the coexistence between a flowing region and a region moving as a whole, similar to what has been observed for bi- or tridimensional shear flows of emulsions [3], colloids [4] or wet granular materials [5–8].

Most of these studies reveal either a continuous [1, 5–7] or discontinuous [2–4] transition between the flowing and non-flowing regions. These differences have not been understood yet and continue to excite debate [2, 9]. A scalar visco-elasto-plastic model including viscous drag [10,11] successfully reproduced the exponential decay of velocity that was observed in the bidimensional plane [9] and cylindrical [1] Couette flows of a foam between two glass plates. In both cases, the localisation was interpreted as the competition between the internal viscosity of the foam and the external friction from the glass plates. Recently, the data presented in [1] were re-analysed in [12] and, in addition to the velocity field, two pieces of tensorial information were extracted both in stationary and transient regimes: the statistical elastic strain tensor and the plastic rearrangements rate tensor. Up to now, these measurements have not been compared yet to a prediction from a numerical model.

The aim of this paper is to compare the measurements on a bidimensional Couette flow of a liquid foam between two glass plates presented in [1,12] with the present numerical computations based on a recent general tensorial and tridimensional visco-elasto-plastic model based on continuous mechanics [13] that combines viscoelasticity and viscoplasticity in a unified framework. This model, which obeys by construction the second principle of thermodynamics, leads to numerically stable equations and robust resolution algorithms. It is general enough to apply to both bi- and tridimensional geometries and to several materials. Here, it is applied to bidimensional foams using three parameters found in the literature (with only minor adjustments) and agrees with the published experiments. This implies that we can also use it to predict flows in several geometries and conditions, including transient, steady and oscillatory flows, even if no experiment is available.

The bidimensional Couette flow experimental set-up discussed here is briefly recalled in the first section. The second section presents the numerical modelling. The numerical results are then analysed and compared with data measurements in the third section for the transient case, and in the fourth section for the stationary case. Finally, the fifth section explores the mechanism of localisation.

[a] e-mail: pierre.saramito@imag.fr
[b] *Present address*: Physics of Geological Processes, University of Oslo, Sem Selands vei 24 NO-0316 Oslo, Norway.

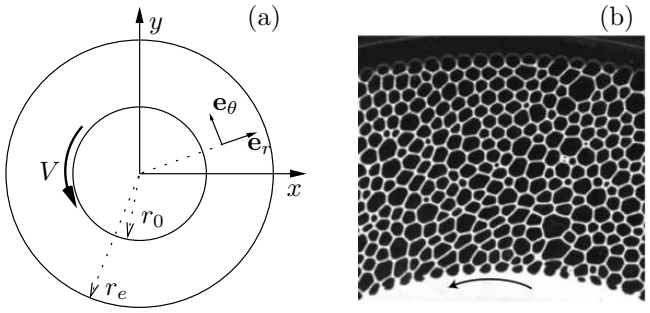

Fig. 1. Experimental set-up: (a) definition of the geometric and kinematic parameters; (b) picture of the confined bidimensional liquid foam (from [1]).

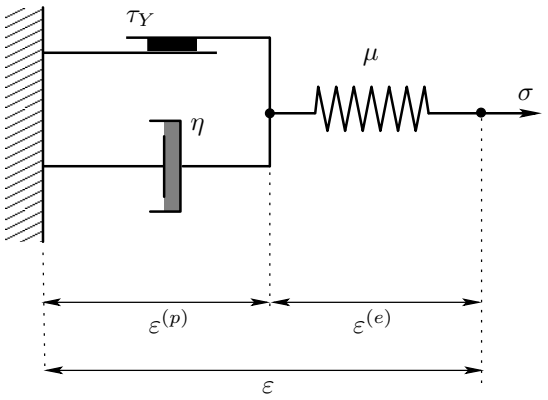

Fig. 2. The visco-elasto-plastic model.

1 Presentation of the experimental set-up

Georges Debrégeas courteously provided data from the experimental set-up represented in Figure 1. It consists of an inner shearing wheel of radius r_0 and an outer fixed one of radius r_e. Let $\Delta r = r_e - r_0$ denote the cylinder gap. The cylinder boundaries are tooth shaped and there is no slip. The liquid fraction (5.2%) is homogeneous and the bubble size is of the order of 2 mm. The foam is confined between two transparent glass plates separated by an interval $h = 2\,\mathrm{mm}$. The inner wheel rotates at $V = 0.25\,\mathrm{mm\,s^{-1}}$, well in the low velocity limit.

Two experimental runs are available:

- *Run* 1 is related to the *transient case*, measurements are available in [12]. The internal radius is $r_0 = 71\,\mathrm{mm}$ and the external radius is $r_e = 112\,\mathrm{mm}$. To prepare the foam, the inner disk is rotated counterclockwise, until a stationary regime is reached; then, at an arbitrary time chosen as the origin ($t = 0$), the shear direction is switched to clockwise, the experiment begins and measurements are made using image analysis. In [12], the measured quantities are averaged over eight equispaced orthoradial circular boxes corresponding to positions $r_j = r_0 + 1.7\,10^{-3} \times (0.4 + 2.7 \times (j - 0.5))$ for $j = 1$ to 8.
- *Run* 2 focuses on the *stationary case* and measurements are presented in [1,12,14]. The internal radius is $r_0 = 71\,\mathrm{mm}$, as for the previous run, and the external radius is $r_e = 122\,\mathrm{mm}$, which differs from the previous run. The preparatory rotation is clockwise. Then, at an arbitrary time, it is switched to counterclockwise. Pictures are recorded only after a full 2π turn.

2 The numerical modelling

The strain tensor $\boldsymbol{\varepsilon}$ is supposed to split into two contributions

$$\boldsymbol{\varepsilon} = \boldsymbol{\varepsilon}^{(p)} + \boldsymbol{\varepsilon}^{(e)}\,, \tag{1}$$

where $\boldsymbol{\varepsilon}^{(p)}$ and $\boldsymbol{\varepsilon}^{(e)}$ denote, respectively, the plastic and the elastic strain tensors. The model considered in this paper is presented in Figure 2. The total Cauchy stress tensor writes

$$\boldsymbol{\sigma} = -p \cdot \boldsymbol{I} + \boldsymbol{\tau}\,, \tag{2}$$

where p is the pressure, $\boldsymbol{I}$ is the identity tensor (here in two dimensions), $\boldsymbol{\tau} = 2\mu\boldsymbol{\varepsilon}^{(e)}$ is the elastic stress tensor, and μ is the elastic modulus of the foam. When the stress is lower than a yield value, the material behaves as an elastic solid: the plastic strain $\boldsymbol{\varepsilon}^{(p)}$ is equal to zero and the stress is $2\mu\boldsymbol{\varepsilon}$. Otherwise, the foam is supposed to behave as a Maxwell viscoelastic fluid with a relaxation time $\lambda = \eta/\mu$, where η is the viscosity.

This model is a simplified version of the model introduced in [13]: the second *solvent* viscosity of the original model is here taken to zero. This choice is coherent with experimental observations [12,15]: at slow strain rate and when no plasticity occurs, the foam behaves as a solid elastic body while the model considered in [13] describes a more general Kelvin-Voigt viscoelastic solid. This choice in the modelling is also justified *a posteriori* in the present paper by comparisons between numerical computations and experimental measurements.

The tensor τ satisfies the following non-linear differential constitutive equation

$$\lambda \frac{\mathcal{D}\boldsymbol{\tau}}{\mathcal{D}t} + \max\left(0,\, 1 - \frac{\tau_Y}{|\boldsymbol{\tau}_d|}\right)\tau = 2\eta \boldsymbol{D}(\mathbf{v}), \tag{3}$$

where $\mathbf{v}$ is the velocity field, $\boldsymbol{D}(\mathbf{v}) = (\nabla\mathbf{v} + \nabla\mathbf{v}^T)/2$ is the strain rate tensor and $\tau_Y > 0$ is the yield stress. We denote also by $\boldsymbol{\tau}_d = \boldsymbol{\tau} - (1/2)\,\mathrm{tr}(\boldsymbol{\tau})\,\boldsymbol{I}$ the deviatoric part of $\boldsymbol{\tau}$ and by $|\boldsymbol{\tau}_d|$ its matrix norm. The upper convected derivative of tensors writes

$$\frac{\mathcal{D}\boldsymbol{\tau}}{\mathcal{D}t} = \frac{\partial\boldsymbol{\tau}}{\partial t} + (\mathbf{v}\cdot\nabla)\boldsymbol{\tau} - \boldsymbol{\tau}\,\nabla\mathbf{v}^T - \nabla\mathbf{v}\,\boldsymbol{\tau}.$$

The set of equations is closed by the conservation of momentum

$$\rho\left(\frac{\partial\mathbf{v}}{\partial t} + \mathbf{v}\cdot\nabla\mathbf{v}\right) - \mathrm{div}\,\boldsymbol{\sigma} = -\frac{\beta}{h}\mathbf{v}, \tag{4}$$

where ρ denotes the density, which is constant [16]. The right-hand side expresses the external force due to the friction of the plates: $\beta \geq 0$ is a friction coefficient and h the distance between the two plates; following [10], a linear friction model is assumed for the sake of simplicity.

A discussion on the effect of this approximation at low velocity can be found in [17]. Finally, since the density is constant, the mass conservation reduces to

$$\operatorname{div} \mathbf{v} = 0. \tag{5}$$

The three unknowns of the problem are $(\boldsymbol{\tau}, \mathbf{v}, p)$ and the corresponding equations are (3), (4) and (5). They are completed by some boundary conditions for $\mathbf{v}$ at $r = r_0$ and r_e for any $t > 0$, and some initial conditions for $\boldsymbol{\tau}$ and $\mathbf{v}$ at $t = 0$. In the bidimensional polar coordinate system (r, θ), we assume the solution to be independent of θ: the radial component velocity v_r is zero and v_θ is simply written as v. Detailed equations presented in Appendix A show that the problem reduces to a time-dependent one-dimensional system of partial derivative equations with four scalar unknowns v, τ_{rr}, $\tau_{r\theta}$, $\tau_{\theta\theta}$ that depend upon t and r.

We solve it with a second-order time splitting algorithm, similar to what has been used for viscoelastic fluid flows problems [18]; this algorithm allows to simplify the highly non-linear initial problem into a sequel of i) elliptic problems resolutions and of ii) constitutive equation resolutions. Problems i) and ii) can then be solved by classical methods. A mixed finite-element method is implemented for the discretisation with respect with r; the gap $[r_0, r_e]$ is discretised with 500 points. The time discretisation is performed with a time step Δt of the order of 0.2 s, which is small considering that the motion is very slow. The stationary solutions are obtained by running the transient algorithm until the relative error between two time steps divided by Δt is less than 10^{-3}.

In order to perform computations and compare them to the experimental data, we need to specify the numerical values of the kinematic and geometric parameters $(V, \Delta r, h)$ of the experimental set-up, and the material parameters $(\mu, \eta, \tau_Y, \beta)$. Let Δr, V, $\Delta r/V$ and $\eta V/\Delta r$ be the characteristic length, velocity, time and stress, respectively. We can define a Reynolds number $Re = \rho V \Delta R/\eta$, but we will see below that we can neglect it. We choose three dimensionless numbers: the Bingham and Weissenberg numbers, and a friction coefficient, defined as, respectively,

$$Bi = \frac{\tau_Y \Delta r}{\eta V}, \qquad We = \frac{\eta V}{\mu \Delta r} \quad \text{and} \quad C_F = \frac{\beta \Delta r^2}{\eta h}. \tag{6}$$

This choice of dimensionless numbers (Bi, We, C_F) corresponds to a description of the foam as a fluid: the characteristic stress is a viscous stress $\eta V/\Delta r$. An alternative choice would be to choose the elastic modulus μ as the characteristic stress, in order to emphasise the elastic-like behaviour of the foam; the corresponding dimensionless numbers would be the yield deformation $\varepsilon_Y^{(e)} = 1/2 Bi\, We = \tau_Y/(2\mu)$, the ratio $\beta V \Delta r/(\mu h) = C_F\, We$ of the friction of the plates with the elastic modulus, and the same Weissenberg number. We will see in the sequel that the latter choice is appropriate for the transient flow description (Sect. 3), whereas the former choice is appropriate for the stationary flow description (Sect. 4).

Table 1. The choice of dimensionless numbers as defined in (6). The material parameters of the foam are identical in both runs, but since the cylinder gaps differ, the dimensionless numbers differ as well.

Run		Bi	We	C_F
1.	transient	68.3	7.31×10^{-3}	39.2
2.	stationary	85.0	5.88×10^{-3}	60.7

From [19], the bidimensional elastic modulus in $\mathrm{N\,m^{-1}}$ is expressed as $\bar{\mu} = \mu/h \approx 2 \cdot 10^{-2}\,\mathrm{N\,m^{-1}}$. The estimation of the elastic modulus μ is thus $\mu \approx 10\,\mathrm{N\,m^{-2}}$. From [15] the relaxation time $\lambda = \eta/\mu$ of the foam on this experiment should be of the order of 1 s, and thus $\eta \approx 10\,\mathrm{Pa\,s}$. The yield strain $\varepsilon_Y^{(e)}$ is dimensionless; it is evaluated from the experiments [12] as the maximal value of $|\boldsymbol{\varepsilon}_d^{(e)}|$ (Fig. 10): $\varepsilon_Y^{(e)} \approx 0.26$, and thus $\tau_Y \approx 5.2\,\mathrm{N\,m^{-2}}$. It should be pointed out that in the model, $|\boldsymbol{\varepsilon}_d^{(e)}|$ can exceed $\varepsilon_Y^{(e)}$ at non-zero velocity. Again from [19], the friction force of the plates is estimated in $\mathrm{N\,m^{-2}}$ for any velocity v as $f = 31\, v^{0.64}$. Since the maximum value of the velocity is $V = 0.25\,\mathrm{mm\,s^{-1}}$, the maximum value of the friction force is $31 \times (0.25 \cdot 10^{-3})^{0.64}$. As we have chosen a linear friction model for the sake of simplicity, $\tilde{f} = \beta v/h$, we choose β such that the maximal value of the friction is the same with both expressions: $\beta \approx 31 \times (0.25 \cdot 10^{-3})^{0.64}/(0.25 \cdot 10^{-3}) = 613\,\mathrm{Pa\,s\,m^{-1}}$.

After a first computation based on this set of parameters, we found a good agreement of the model with *both* transient and stationary cases with slightly adjusted parameters which we use throughout the paper for comparison with experiments: $\mu = 10.9\,\mathrm{N\,m^{-2}}$, $\eta = 13.1\,\mathrm{Pa\,s}$, $\tau_Y = 5.47\,\mathrm{N\,m^{-2}}$. $\beta = 613\,\mathrm{Pa\,s\,m^{-1}}$. This adjustment leads to the set of dimensionless numbers (6) presented in Table 1.

Since the non-linear inertia term $\mathbf{v} \cdot \nabla \mathbf{v}$ in (4) vanishes for simple shear flows such as the Couette flow, the Reynolds number $Re = \rho V \Delta r/\eta \approx 5 \times 10^{-5}$ has a negligible influence on the transient problem and no influence on the stationary one. Thus, Re is taken as zero for the computations. For the comparison with experiments, the results at time t and radius r are expressed in a dimensionless form, respectively, as the total applied shear $\gamma = Vt/\Delta r$ and as the distance to the inner cylinder normalised by the size of the gap $(r - r_0)/\Delta r$.

3 The transient flow

The transient numerical computation is performed as follows: first, the computation is done with the foam initially at rest with $v(r_0) = V$ and $v(r_e) = 0$. When a stationary regime is reached, the boundary conditions are changed to $v(r_0) = -V$ and $v(r_e) = 0$ at a time chosen as the origin $(t = 0)$ and results are stored at each time step.

Figure 3a plots the velocity profile *versus* r at different times. Conversely, the velocity is represented in Figure 3b

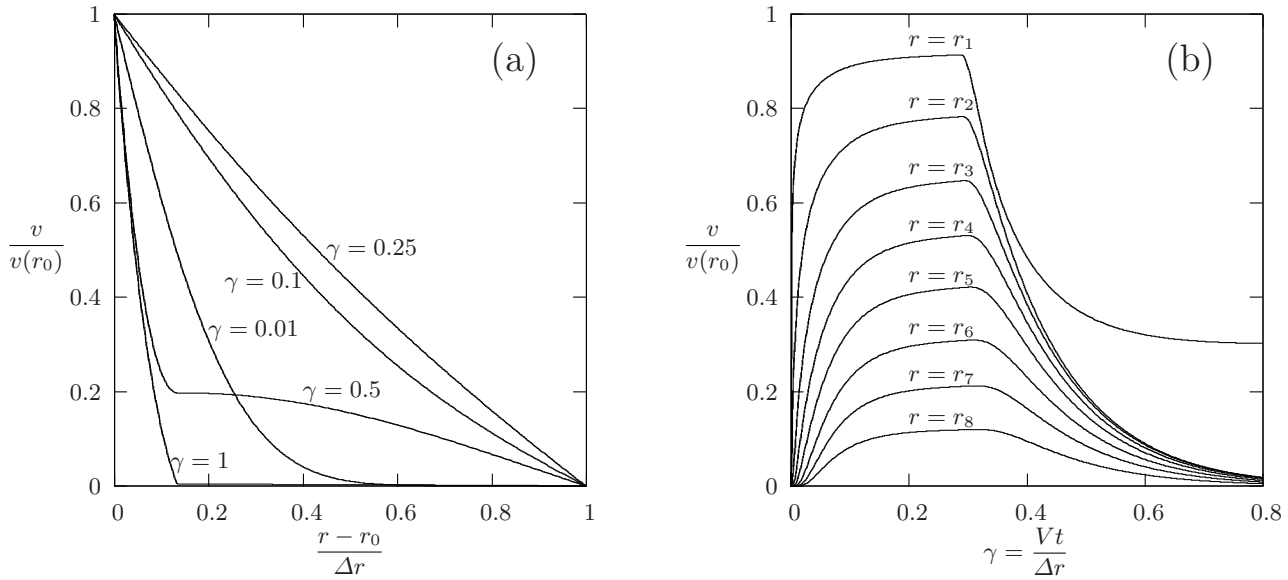

Fig. 3. Transient case. (a) Velocity profile *versus* r at different times; (b) velocity profile *versus* t for $r = r_1$ to r_8.

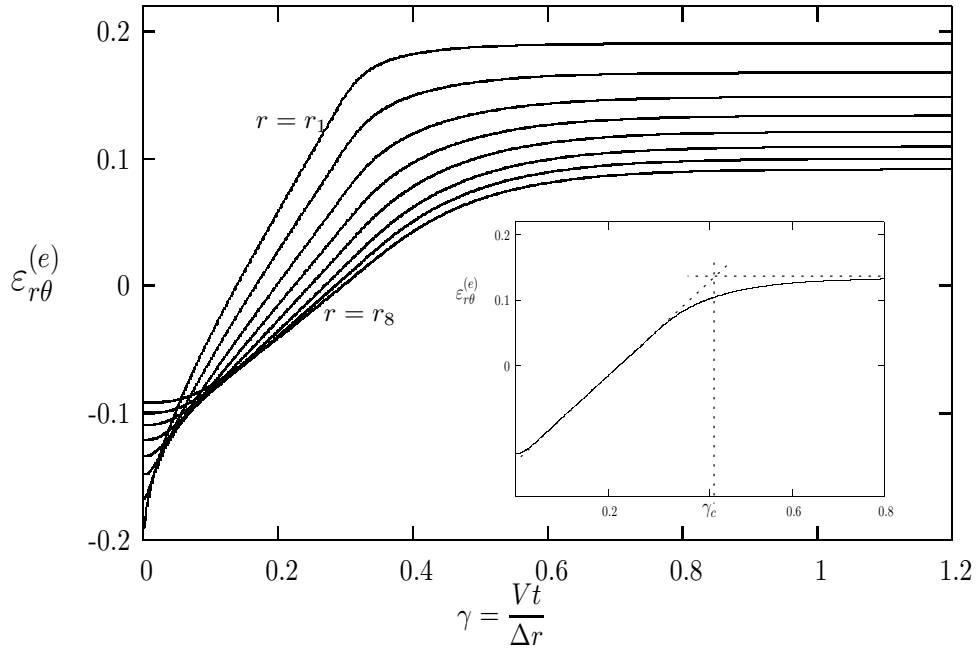

Fig. 4. Transient case. Cross-component of the elastic strain $\varepsilon^{(e)}_{r\theta}$ *versus* t for $r = r_1$ to r_8. Inset: the vertical dashed line marks the cross-over γ_c between the transient and the stationary regimes, defined by the intersection of the tangent at the point of minimum curvature and the asymptotic value of $\varepsilon^{(e)}_{r\theta}$, here plotted for $r = r_4$.

versus time at different radii, from $r = r_1$ to r_8. When $\gamma = 0.01$, the shear direction has just been switched and the velocity profile is roughly exponential. After a short transient, $0 \leq \gamma \leq 0.1$, the velocity profile becomes quasi-linear up to $\gamma \approx 0.3$. Then, at $\gamma = 0.3$ and $r = r_1$, *i.e.* near the moving disk, it starts to decrease rather abruptly. Far from the moving disk, the decreasing starts later, at $\gamma = 0.35$. At $\gamma = 1$, the foam has reached a stationary regime in which the flow is strongly localised near the moving disk.

Figure 4 shows $\varepsilon^{(e)}_{r\theta} = \tau_{r\theta}/2\mu$ *versus* time for $r = r_1$ to r_8. After a short transient of about 0.05, $\varepsilon^{(e)}_{r\theta}$ reaches a first regime where it varies linearly ($0.05 \leq \gamma \leq 0.3$ for $r = r_1$ and $0.2 \leq \gamma \leq 0.4$ for $r = r_8$). Thus, the stress τ depends linearly upon γ, *i.e.* the material behaves as an elastic solid in this regime. Then, after a second transition, τ saturates and reaches a stationary regime. For a given radius r, the characteristic value of γ associated to this second transition is denoted by $\gamma_c(r)$, defined as the intersection between the tangent at the point of minimal

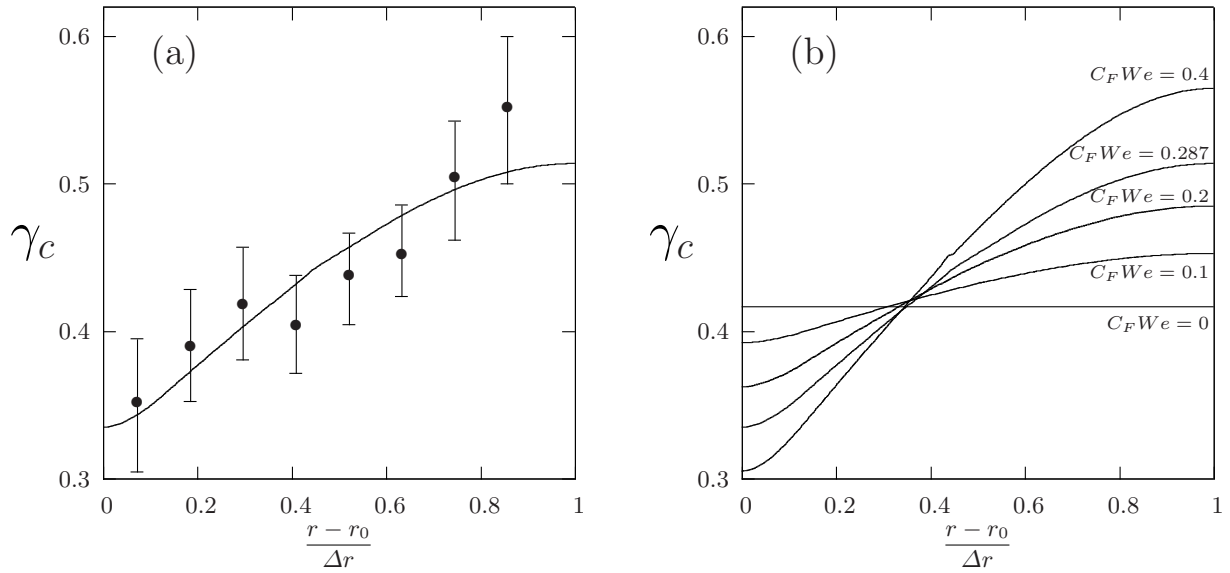

Fig. 5. Transient case. (a) γ_c *versus* r with parameters as in Table 1. Solid dots: experimental data with error bars; solid line: numerical data. (b) γ_c *versus* r with Bi and We as in Table 1 and $C_FWe = 0$, 0.1, 0.2, 0.287, 0.4.

curvature in the transient regime and the horizontal line corresponding to the asymptotic value in the stationary regime, as shown in the inset of Figure 4.

Figure 5a shows the inhomogeneity in yielding across the gap. The numerical results agree with the experiment [12] within error bars. Both numerical and experimental results show that the regions close to the moving wall saturate earlier than the regions far from it. We take advantage of the numerical computations to study how this inhomogeneity depends on the physical parameters. As mentioned in Section 2, the appropriate parameters here are $(BiWe, C_FWe, We)$. We find that when $C_FWe = 0.287$ is maintained constant and $BiWe$ and We are varying, the curve $\gamma_c(r)$ is only translated upwards or downwards, the inhomogeneity throughout the gap remains the same. Conversely, when $BiWe$ and We are fixed as in Table 1, the inhomogeneity varies with C_FWe (see Fig. 5b). We plot in Figure 6 $\gamma_c(r_e) - \gamma_c(r_0)$ *versus* C_FWe; the dependence is almost linear:

$$\gamma_c(r_e) - \gamma_c(r_0) \approx 0.65\, C_FWe. \tag{7}$$

In particular, when $C_FWe = 0$, $\gamma_c(r) = 0$ for all r; the inhomogeneity is thus an effect of the friction of the plates.

Figure 7 plots the norm of the deviatoric part of the elastic strain tensor

$$\left|\boldsymbol{\varepsilon}_d^{(e)}\right| = \left[2\left(\varepsilon_{r\theta}^{(e)}\right)^2 + \frac{1}{2}\left(\varepsilon_{rr}^{(e)} - \varepsilon_{\theta\theta}^{(e)}\right)^2\right]^{\frac{1}{2}}.$$

We recall that the plasticity occurs when $|\boldsymbol{\tau}_d| \geq \tau_Y$, and thus when $|\boldsymbol{\varepsilon}_d^{(e)}|$ is above $\varepsilon_Y^{(e)} = \tau_Y/(2\mu) = Bi\, We/2 = 0.25$. Figure 7 shows that it occurs only close to the moving cylinder, for $r = r_1$; and only for small times, during the first transition regime, or for large time, during the stationary regime. At initial time, $|\boldsymbol{\varepsilon}_d^{(e)}|$ is above $\varepsilon_Y^{(e)}$ near the moving disk. As the disk moves, the velocity and its gradient change sign and $|\boldsymbol{\varepsilon}_d^{(e)}|$ decreases rapidly until $|\boldsymbol{\varepsilon}_d^{(e)}| < \varepsilon_Y^{(e)}$ everywhere in the foam. Therefore there is no plasticity in the foam and the constitutive equation (3) reduces to $\mathcal{D}\boldsymbol{\varepsilon}^{(e)}/\mathcal{D}t = D(\mathbf{v})$. This relation expresses that all the velocity gradient is loaded into $\boldsymbol{\varepsilon}^{(e)}$. The foam behaves like an elastic body and $\varepsilon_{r\theta}^{(e)}$ increases linearly with the applied strain γ. Because of the cylindric geometry and the friction of the plates, $\boldsymbol{\varepsilon}^{(e)}$ is higher near the inner moving disk. When $|\boldsymbol{\varepsilon}_d^{(e)}|$ reaches $\varepsilon_Y^{(e)}$ near the inner disk, plasticity occurs and the foam starts to flow. Then $\boldsymbol{\varepsilon}^{(e)}$ saturates everywhere in the gap, even though it is above the yield deformation only in a region near the moving

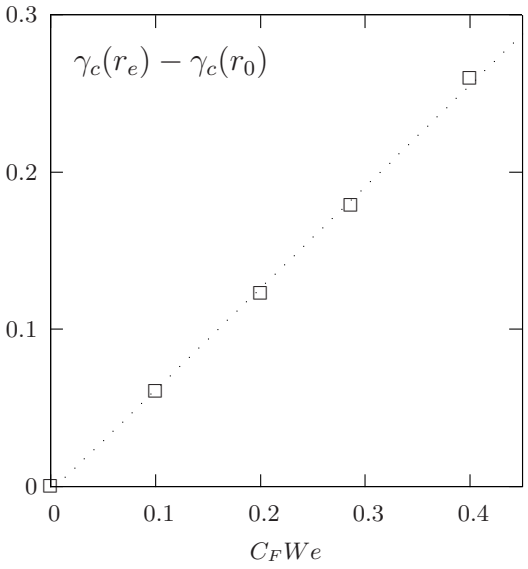

Fig. 6. Transient case. $\gamma_c(r_e) - \gamma_c(r_0)$ *versus* C_FWe. Open squares: numerical data; dotted line: linear fit to these data.

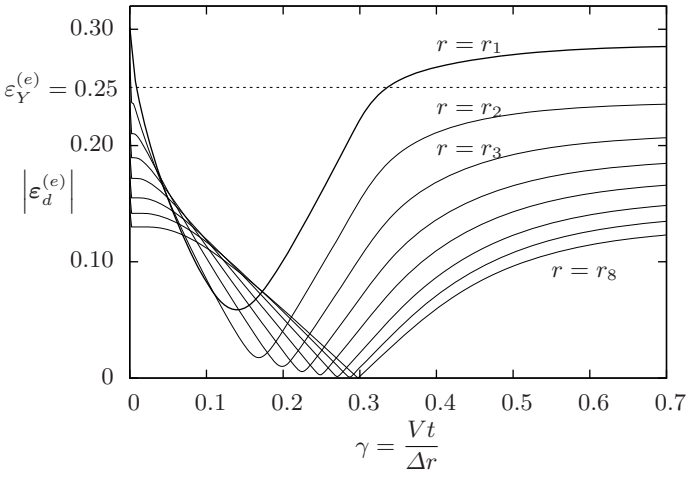

Fig. 7. Transient case. $|\boldsymbol{\varepsilon}_d^{(e)}|$ *versus* t for r from $r = r_1$ to r_8.

disk. Inside this region, the foam is flowing, while outside there is no flow and the foam is at rest.

Let us summarise our findings for the transient case. After a brief transient, the material behaves as an elastic solid: there is no plasticity yet and the velocity profile is quasi-linear. The deformation saturates first near the moving disk, and then gradually throughout the gap. The friction of the plates is responsible for this gradual saturation. Finally, after this second transient, the stationary regime is reached: the material is flowing and the flow is strongly localised near the moving disk.

4 The stationary flow

The stationary numerical computation is performed as follows: as in the experiment, there is a preparatory clockwise rotation (the boundary conditions are $v(r_0) = -V$ and $v(r_e) = 0$) after which the inner cylinder is rotated counterclockwise (the boundary conditions become $v(r_0) = V$ and $v(r_e) = 0$). As in the previous section, after a transient, the flow evolves asymptotically and monotonously towards a stationary flow.

Figure 8a compares the numerical results to measurements made in [1]. The velocity is strongly localised near the moving disk, as in the transient case (Fig. 3a). Both the computed and experimental velocities have the same initial slope, but the transition to zero is more abrupt in the case of the numerical resolution. We denote by r_c the radius at which the velocity drops to zero. The computation yields $r_c = 77.6\,\mathrm{mm}$ while $r_c = 84.0\,\mathrm{mm}$ for the experimental data. The r_c prediction error is about 12% of the gap size. The origin of this abrupt behaviour is discussed in the sequel.

Figure 8b represents the total shear strain rate $\dot{\varepsilon}_{r\theta}$: it strongly localises near the moving disk, and is discontinuous at the transition between the flowing and non-flowing regions. There is no experimental data available for the comparison.

The stationary elastic strain $\boldsymbol{\varepsilon}^{(e)}$ (Fig. 9) is compared to experimental measurements from [12]. The computed shear component $\varepsilon_{r\theta}^{(e)}$ (Fig. 9a) is slightly overestimated. Nevertheless, it presents qualitatively the same behaviour as in the experiment: it does not localise near the moving disk and varies smoothly with r. The computed difference of the normal components $\varepsilon_{rr}^{(e)} - \varepsilon_{\theta\theta}^{(e)}$ presents a discontinuity at the point at $r = r_c$, where the computed velocity and plasticity drop to zero (Fig. 9b). Conversely, the sign of the experimental data changes in the middle of the gap. This strong difference is not surprising since $\varepsilon_{rr}^{(e)} - \varepsilon_{\theta\theta}^{(e)}$ is not so geometrically constrained as is $\varepsilon_{r\theta}^{(e)}$, and depends on the foam preparation. This is especially true in the region of the foam which is not sheared much beyond the plasticity limit. Anisotropic trapped elasticity [20] may be initially present in the experimental set-up [12]. Similarly, in the model, the stationary normal components depend on the initial conditions (cf. Appendix B).

Finally, we plot $|\boldsymbol{\varepsilon}_d^{(e)}|$ *versus* r (Fig. 10); this quantity is discontinuous as well; $\max(0, 1 - \tau_Y/|\boldsymbol{\tau}_d|)$ is zero for $r = r_c^+$ but non zero for $r = r_c^-$.

Such an abrupt transition has been observed on bubble rafts [2] and various experimental systems [3,4]. In the present numerical computation, this discontinuity is an effect of the model and not a numerical artefact. Calculations presented in Appendix B show that in the stationary regime the model analytically predicts either continuous or discontinuous quantities, separated by a critical strain rate

$$\dot{\varepsilon}_{r\theta}^c \frac{\tau_{r\theta}(r_c)}{2\eta} \left[1 - \frac{\tau_Y}{\sqrt{2}|\tau_{r\theta}(r_c)|} \frac{1}{\left(1 + \frac{\lambda^2}{\eta^2}\tau_{r\theta}(r_c)^2\right)^{1/2}} \right]. \quad (8)$$

If we assume that the normal stress difference is small compared to the shear stress in the non-flowing, elastic region, then $|\tau_{r\theta}(r_c)|$ is of the order of $\tau_Y/\sqrt{2}$ and (8) yields a more practical formula that does not involve $\tau_{r\theta}(r_c)$

$$|\dot{\varepsilon}_{r\theta}^c| \approx \frac{\sqrt{2}\tau_Y}{4\eta} \left[1 - \frac{1}{\left(1 + \frac{\lambda^2}{2\eta^2}\tau_Y^2\right)^{1/2}} \right]. \quad (9)$$

Equation (9) yields $\Delta r/v(r_0)|\dot{\varepsilon}_{r\theta}^c| = 1.72$, in excellent agreement with the computed value (Fig. 8b) $\Delta r/v(r_0)|\dot{\varepsilon}_{r\theta}^c| = 1.73$.

If we set $\lambda = 0$ in (3), the model reduces to the Bingham model; if we set $\tau_Y = 0$ in (3), the model reduces to the Oldroyd-B model. None of these models exhibits a critical strain rate whereas their combination does. When λ is not zero, the term $-\boldsymbol{\tau}\nabla\mathbf{v}^t - \nabla\mathbf{v}\boldsymbol{\tau}$ in the objective derivative introduces normal components in the off-diagonal term of the constitutive equation (cf. Appendix A) which enables the model to have discontinuous solutions even though the term $\max(0, 1 - \tau_Y/|\boldsymbol{\tau}_d|)\tau$ is continuous. Thus, the discontinuous behaviour observed with the present model arises from the tensorial formalism. A scalar model may not be able to reproduce it.

Let us summarise our findings in the stationary case. The flowing region is well predicted by the model. The non-flowing region is very sensitive, especially to foam

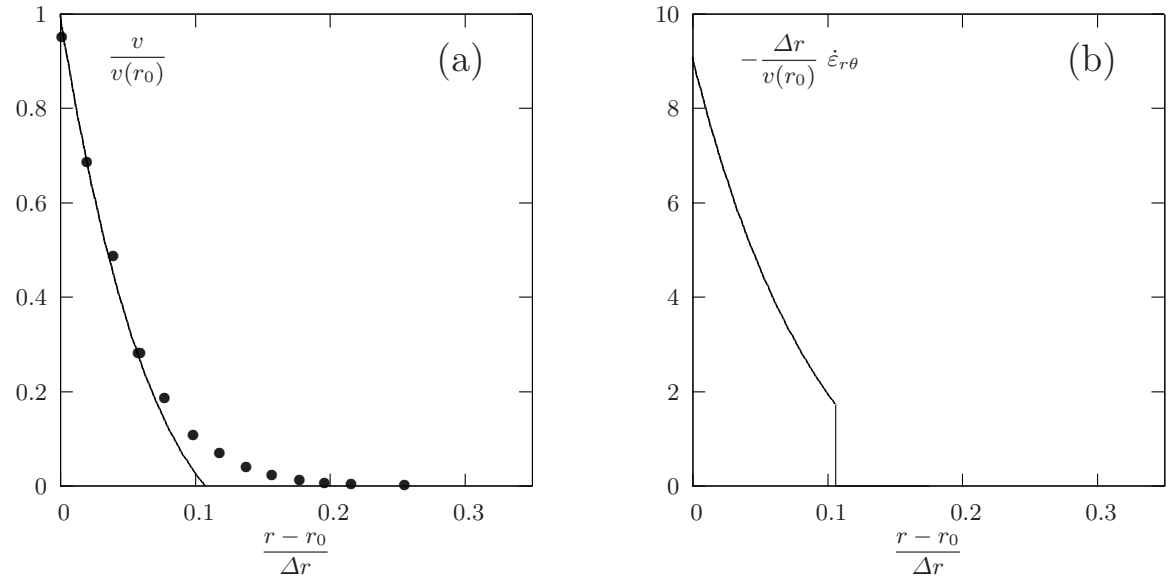

Fig. 8. Stationary case. (a) Velocity *versus* r. Solid line: computation; solid dots: experimental data from [1]. (b) Shear strain rate $\dot{\varepsilon}_{r\theta}$ *versus* r. There is no experimental data available for the comparison.

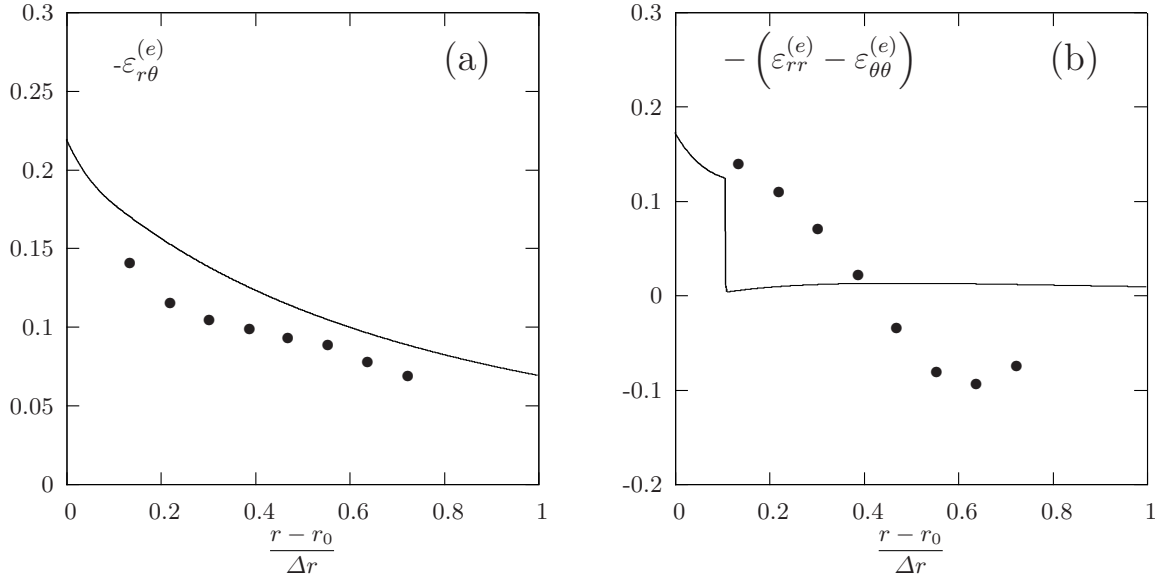

Fig. 9. Stationary case. Solid line: numerical resolution; solid dots: experimental data from [12]. (a) Shear component $-\varepsilon^{(e)}_{r\theta}$ *versus* r. (b) Difference of normal components $-(\varepsilon^{(e)}_{rr}-\varepsilon^{(e)}_{\theta\theta})$ *versus* r.

preparation, both in the experiments and in the model. In between, the model can predict a discontinuous transition. In this case, we are able to predict the velocity gradient jump.

5 The mechanism of localisation

In order to probe the effect of the friction of the plates on the localisation in the stationary regime, a stationary numerical computation with both $Bi = 85.0$ and $We = 5.88 \times 10^{-3}$ unchanged, and C_F set to zero, is performed. The result is compared (Fig. 11a) with the numerical solution with the reference set of parameters $C_F = 60.7$ from Table 1. The velocity profile is almost the same: the friction of the plates does not seem to be responsible for the localisation in this experiment. The dependence of the localisation point r_c upon We was found to be negligible. More precisely, for any fixed value of Bi in the range $[0 : 153]$, the variation of $r_c/\Delta r$ upon We in the range $[0 : 1.96 \times 10^{-2}]$ was found to be less than 3%. Therefore, the localisation point r_c can be approximated using the Bingham model.

Figure 11b plots the localisation point *versus* Bi for the Bingham model ($We = C_F = 0$): $r_c - r_0$ behaves as $Bi^{-1/2}$. An explicit computation for the Couette flow of

a Bingham fluid (see, *e.g.*, [21] or p. 241 of [22]) expresses the ratio r_c/r_0 as the solution of

$$\left(\frac{r_c}{r_0}\right)^2 - 2\ln\left(\frac{r_c}{r_0}\right) = 1 + 2\sqrt{2}\left(\frac{\Delta r}{r_0}\right) Bi^{-1}. \qquad (10)$$

A Taylor expansion of (10) for small $r_c - r_0$ leads to

$$\frac{r_c - r_0}{\Delta r} \approx 2^{1/4}\left(\frac{r_0}{\Delta r}\right)^{1/2} Bi^{-1/2}. \qquad (11)$$

This explicit approximate formula predicts well the localisation point, as shown in Figure 11b.

In [9], the authors shear a bubble raft in a *plane* Couette geometry and see no localisation at all. Adding a plate on the top, a localisation is observed. The authors conclude that the plate is responsible for the localisation. This result seems to be in contradiction with our conclusion that the friction has a minor influence on the localisation. Therefore, we performed the numerical resolution of our model in the case of a *plane* Couette flow, in order to check if our model was able to reproduce the behaviour observed in [9]. We used a gap width of 40 mm and a moving boundary with a velocity of 0.25 mm/s as in [9]. The dimensionless numbers $Bi = 85$ and $We = 5.88 \times 10^{-3}$ are fixed and only C_F is varying. Figure 12 shows the results for $C_F = 0$, 6.07 and 60.7. For $C_F = 0$, all the foam is flowing and the velocity profile is linear (Fig. 12a) while $|\boldsymbol{\varepsilon}_d^{(e)}|$ is constant and above $\varepsilon_Y^{(e)}$ (Fig. 12b). For $C_F = 6.07$, all the foam is flowing but the velocity profile is no longer linear, while $|\boldsymbol{\varepsilon}_d^{(e)}|$ is non-uniform but above $\varepsilon_Y^{(e)}$ throughout the gap. For $C_F = 60.7$, the velocity is localised near the moving wall and $|\varepsilon_d^{(e)}|$ is not uniform: it is above $\varepsilon_Y^{(e)}$ in the region where the velocity is not zero and under $\varepsilon_Y^{(e)}$ otherwise.

Let us summarise our findings. We explain the localisation by the non-uniform stress: part of the system is above the yield stress and part of the system is below the yield stress. In the case of the *plane* Couette flow, the friction of the plates is responsible for the non-uniform stress. In the case of the *cylindrical* Couette flow, it is mostly the geometry, and the localisation position is mainly governed by the Bingham number while both the friction and the Weissenberg number have only a minor influence.

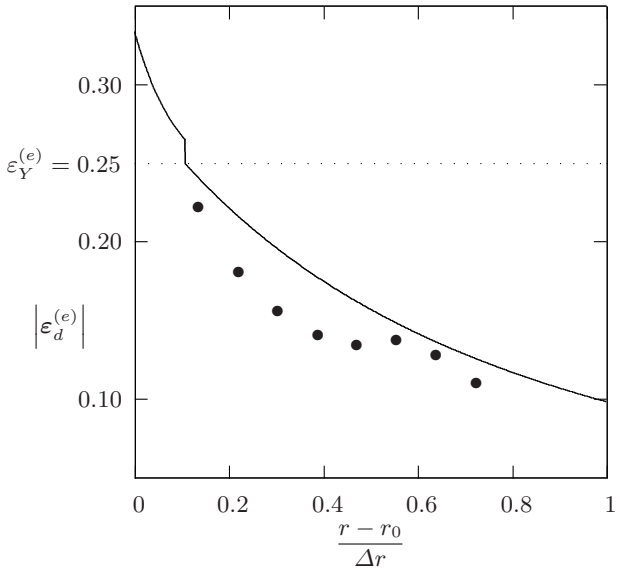

Fig. 10. Stationary case. $|\boldsymbol{\varepsilon}_d^{(e)}|$ *versus* r. Solid line: numerical resolution; solid dots: experimental data from [12].

The transition to the shear banding was analysed both in the transient and stationary cases. An elastic behaviour appears during the transient flow. The effect of the friction of plates on the propagation of the plastic rearrangements throughout the gap is also analysed in details. In the stationary case, a non-uniform stress throughout the gap leads to a flowing part above the yield stress and a non-flowing part under the yield stress. It appears to be the fundamental mechanism for the localisation of the flow. The mechanism of localisation is analysed in details with respect to the effect of friction on the plates and to the plasticity. Finally, the plasticity appears to be the fundamental mechanism of the localisation of the flow.

In the future, we plan to compare the numerical resolution of our model with more complex liquid foam flows like flows around an obstacle. It can also be interesting to study models with a different description of plasticity as in [14]. Finally, we point out the fact that our approach is not specific to liquid foams: it could well describe emulsions, colloids or wet granular materials that are known to develop a similar behaviour.

Conclusion

For the first time, comparisons between a visco-elasto-plastic model based on continuous mechanics and measurements both in stationary and transient cases are performed and found to be in good agreement. The direct numerical resolution enables a full comparison with all available data from measurement. The comparison performed with only one set of material parameters confirms the predictive character of the proposed model. This model is fully parametrised by only three standard dimensionless numbers that depend on a limited set of experimentally measurable material parameters.

We are extremely grateful to G. Debrégeas for providing us with many recordings of his published and unpublished experiments. We would also like to thank S. Cox, B. Dollet, E. Janiaud, A. Wyn, and the Foam Mechanics Workshop (Grenoble, January 2008) and all its participants for fruitful discussions.

Appendix A. Detailed equations

We write equations (3, 4) and (5) in cylindrical coordinates, using the fact that the velocity is of the form $\mathbf{v} = (0, v(t, r))$ and that the $\boldsymbol{\tau}$ tensor components depend only on t and r. The tensorial equation (3) is equivalent

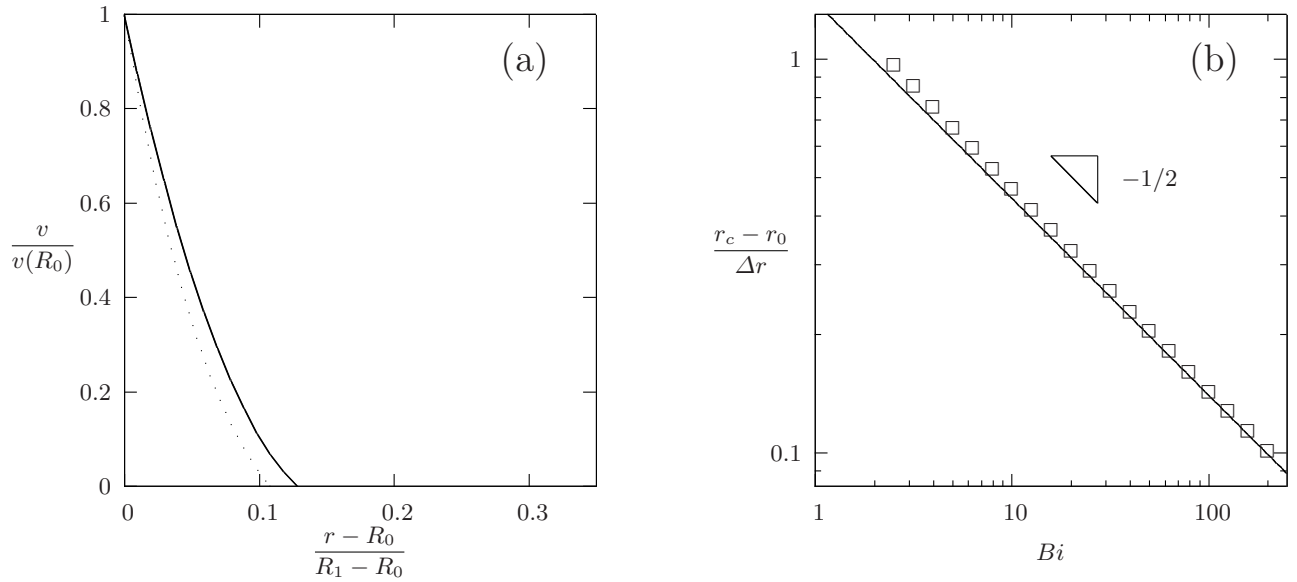

Fig. 11. Stationary case. (a) Velocity profile for $Bi = 85$, $We = 5.88 \times 10^{-3}$; $C_F = 0$ (solid line) or $C_F = 60.7$ (dotted line). (b) Localisation point *versus* Bi for the stationary Bingham fluid ($We = C_F = 0$); open squares: exact analytical result (10); solid line: approximate numerical prediction (11).

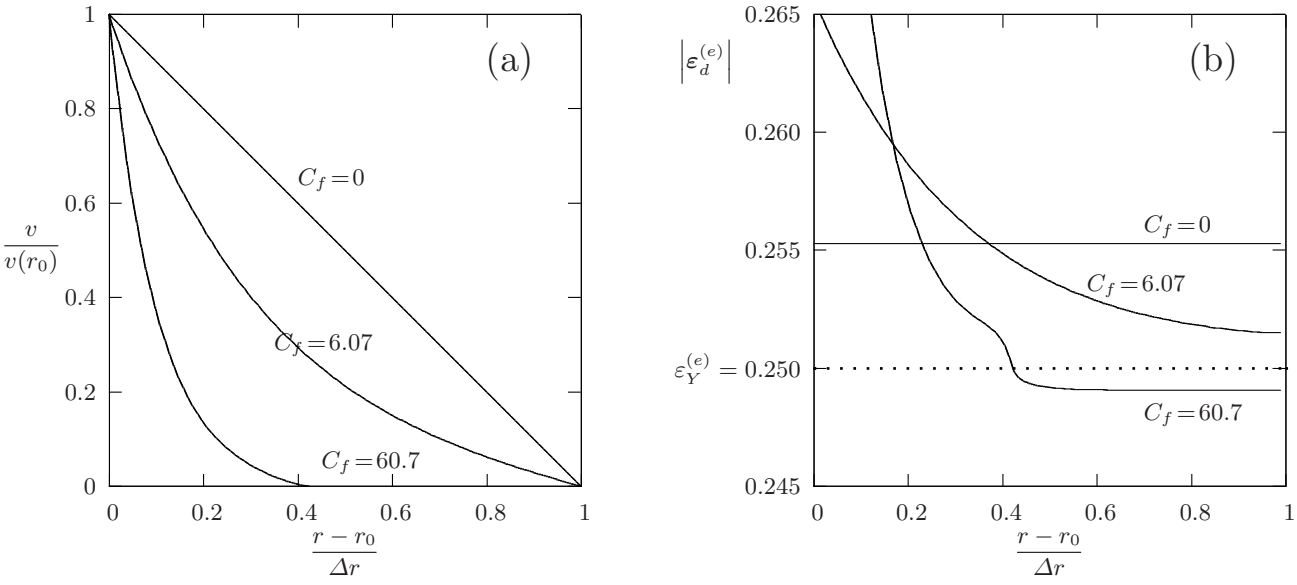

Fig. 12. Stationary plane Couette case with $Bi = 85$, $We = 5.88 \times 10^{-3}$ and C_F varying: (a) velocity profile; (b) $|\boldsymbol{\varepsilon}_d^{(e)}|$.

to three scalar equations:

$$\lambda\left(\frac{\partial\tau_{rr}}{\partial t}+2\frac{v}{r}\tau_{r\theta}\right)+\max\left(0,1-\frac{\tau_Y}{|\boldsymbol{\tau}_d|}\right)\tau_{rr}=0, \quad \text{(A.1a)}$$

$$\lambda\left(\frac{\partial\tau_{r\theta}}{\partial t}-\frac{\partial v}{\partial r}\tau_{rr}+\frac{v}{r}\tau_{\theta\theta}\right)$$
$$+\max\left(0,1-\frac{\tau_Y}{|\boldsymbol{\tau}_d|}\right)\tau_{r\theta}-\eta\left(\frac{\partial v}{\partial r}-\frac{v}{r}\right)=0, \quad \text{(A.1b)}$$

$$\lambda\left(\frac{\partial\tau_{\theta\theta}}{\partial t}-2\frac{\partial v}{\partial r}\tau_{r\theta}\right)+\max\left(0,1-\frac{\tau_Y}{|\boldsymbol{\tau}_d|}\right)\tau_{\theta\theta}=0, \quad \text{(A.1c)}$$

with $|\boldsymbol{\tau}_d| = (2\tau_{r\theta}^2 + \frac{1}{2}(\tau_{rr}-\tau_{\theta\theta})^2)^{1/2}$. The vectorial equation (4) is equivalent to two scalar equations:

$$\frac{\partial p}{\partial r}-\frac{\partial\tau_{rr}}{\partial r}-\frac{\tau_{rr}-\tau_{\theta\theta}}{r}=0, \quad \text{(A.2a)}$$

$$-\frac{1}{r^2}\frac{\partial}{\partial r}\left(r^2\tau_{r\theta}\right)=-\frac{\beta v}{h}. \quad \text{(A.2b)}$$

Equation (5) is verified for any $\mathbf{v}$ of the form $(0, v(r))$.

Appendix B. Analytical analysis of the stationary equations

We show here that the model can lead either to continuous or discontinuous quantities in the stationary regime for the circular geometry. Similar developments can be made for the plane geometry and yield the same results. We make the reasonable assumptions that in the stationary regime, $|\boldsymbol{\tau}_d|$ is decreasing throughout the gap, and that there exists r_c such that $|\boldsymbol{\tau}_d| > \tau_Y$ for $r < r_c$ and $|\boldsymbol{\tau}_d| < \tau_Y$ for $r > r_c$.

First of all, as there are no point forces at the interface between flowing and non-flowing regions, the total stress $\boldsymbol{\tau} - p\mathbf{I}$ has to be continuous. However, this is not necessarily the case for the components of $\boldsymbol{\tau}$: (A.2a) shows that the normal components of $\boldsymbol{\tau}$ can be discontinuous if the pressure is discontinuous; conversely, (A.2b) shows that $\tau_{r\theta}$ must be continuous as it is not balanced with pressure.

Then we write the constitutive equation with $\frac{\partial}{\partial t} = 0$. We have:

- When $r > r_c$: the plasticity term is zero, so (A.1b) leads to $2\lambda(v/r)\tau_{r\theta} = 0$, and $v = 0$ as $\tau_{r\theta} \neq 0$. Equation (A.1c) leads to $-2\lambda\frac{\partial v}{\partial r}\tau_{r\theta} = 0$, and thus $\frac{\partial v}{\partial r} = 0$. However, (A.1b) is then equivalent to $0 = 0$, and the normal stress components are not determined by the stationary equations only. In the transient problem, their values are determined by the initial conditions. Finally, as $v = 0$, (A.2b) yields $\tau_{r\theta} = C/r^2$, where C is a constant.
- When $r < r_c$: (A.1b-A.1c) lead to

$$
\begin{aligned}
&2\lambda\frac{v}{r}\tau_{r\theta} + \left(1 - \frac{\tau_Y}{|\boldsymbol{\tau}_d|}\right)\tau_{rr} = 0,\\
&-\lambda\left(\frac{\partial v}{\partial r}\tau_{rr} - \frac{v}{r}\tau_{\theta\theta}\right) + \left(1 - \frac{\tau_Y}{|\boldsymbol{\tau}_d|}\right)\tau_{r\theta} = \eta\left(\frac{\partial v}{\partial r} - \frac{v}{r}\right),\\
&-2\lambda\frac{\partial v}{\partial r}\tau_{r\theta} + \left(1 - \frac{\tau_Y}{|\boldsymbol{\tau}_d|}\right)\tau_{\theta\theta} = 0.
\end{aligned}
$$

We denote with a^- (respectively, a^+) the quantities evaluated in $r = r_c^-$ (respectively, in $r = r_c^+$); v and $\tau_{r\theta}$ are continuous, thus $v^- = v^+ = 0$, $\tau_{r\theta}^- = \tau_{r\theta}^+ = \tau_{r\theta}(r_c)$ and we have

$$
\begin{aligned}
&\left(1 - \frac{\tau_Y}{|\boldsymbol{\tau}_d^-|}\right)\tau_{rr}^- = 0,\\
&-\lambda\frac{\partial v}{\partial r}^-\tau_{rr}^- + \left(1 - \frac{\tau_Y}{|\boldsymbol{\tau}_d^-|}\right)\tau_{r\theta}(r_c) = \eta\frac{\partial v}{\partial r}^-,\\
&-2\lambda\frac{\partial v}{\partial r}^-\tau_{r\theta}(r_c) + \left(1 - \frac{\tau_Y}{|\boldsymbol{\tau}_d^-|}\right)\tau_{\theta\theta}^- = 0.
\end{aligned}
$$

If $1 - \frac{\tau_Y}{|\boldsymbol{\tau}_d^-|} = 0$, we find $\frac{\partial v}{\partial r}^- = 0 = \frac{\partial v}{\partial r}^+$: there is no discontinuity.

If $1 - \frac{\tau_Y}{|\boldsymbol{\tau}_d^-|} \neq 0$, we find

$$
\begin{aligned}
\tau_{rr}^- &= 0,\\
\tau_{\theta\theta}^- &= 2\frac{\lambda}{\eta}\tau_{r\theta}(r_c)^2,\\
\frac{\partial v}{\partial r}^- &= \frac{1}{\eta}\left(1 - \frac{\tau_Y}{|\boldsymbol{\tau}_d^-|}\right)\tau_{r\theta}(r_c),
\end{aligned}
$$

with now

$$
|\boldsymbol{\tau}_d^-| = \left(2\tau_{r\theta}(r_c)^2 + 2\frac{\lambda^2}{\eta^2}\tau_{r\theta}(r_c)^4\right)^{1/2}.
$$

As $\frac{\partial v}{\partial r}^- \neq \frac{\partial v}{\partial r}^+$, the strain rate is discontinuous at $r = r_c$ and we can define a critical strain rate

$$
\begin{aligned}
\dot{\varepsilon}_{r\theta}^c &= \frac{1}{2}\left(\frac{\partial v}{\partial r}^- - \frac{v}{r}\right)\\
&= \frac{1}{2\eta}\left[1 - \frac{\tau_Y}{\sqrt{2}|\tau_{r\theta}(r_c)|}\frac{1}{\left(1 + \frac{\lambda^2}{\eta^2}\tau_{r\theta}(r_c)^2\right)^{1/2}}\right]\tau_{r\theta}(r_c).
\end{aligned}
$$

References

1. G. Debrégeas, H. Tabuteau, J.M. di Meglio, Phys. Rev. Lett. **87**, 178305 (2001).
2. J. Lauridsen, G. Chanan, M. Dennin, Phys. Rev. Lett. **93**, 018303 (2004).
3. P. Coussot, J.S. Raynaud, F. Bertrand, P. Moucheront, J.P. Guilbaud, H.T. Huynh, S. Jarny, D. Lesueur, Phys. Rev. Lett. **88**, 218301 (2002).
4. J.B. Salmon, A. Colin, S. Manneville, F. Molino, Phys. Rev. Lett. **90**, 228303 (2003).
5. D. Howell, R.P. Behringer, C. Veje, Phys. Rev. Lett. **82**, 5241 (1999).
6. D.M. Mueth, G.F. Debregeas, G.S. Karczmar, P.J. Eng, S.R. Nagel, H.M. Jaeger, Nature **406**, 385 (2000).
7. W. Losert, L. Bocquet, T.C. Lubensky, J.P. Gollub, Phys. Rev. Lett. **85**, 1428 (2000).
8. N. Huang, G. Ovarlez, F. Bertrand, S. Rodts, P. Coussot, D. Bonn, Phys. Rev. Lett. **94**, 028301 (2005).
9. Y. Wang, K. Krishan, M. Dennin, Phys. Rev. E **73**, 031401 (2006).
10. E. Janiaud, D. Weaire, S. Hutzler, Phys. Rev. Lett. **97**, 038302 (2006).
11. R.J. Clancy, E. Janiaud, D. Weaire, S. Hutzler, Eur. Phys. J. E **21**, 123 (2006).
12. E. Janiaud, F. Graner, J. Fluid Mech. **532**, 243 (2005).
13. P. Saramito, J. Non Newtonian Fluid Mech. **145**, 1 (2007).
14. P. Marmottant, C. Raufaste, F. Graner, Eur. Phys. J. E **25**, 371 (2008).
15. A. Kabla, J. Scheibert, G. Debrégeas, J. Fluid Mech. **587**, 45 (2007).
16. D. Weaire, S. Hutzler, *The Physics of Foams* (Oxford University Press, Oxford, 1999).

17. G. Katgert, M.E. Mobius, M. van Hecke, Phys. Rev. Lett. **101**, 058301 (2008).
18. P. Saramito, J. Non Newtonian Fluid Mech. **60**, 199 (1995).
19. C. Raufaste, Ph.D. Thesis, Université Joseph Fourier, Grenoble, France (2007) `http://tel.archives-ouvertes.fr/docs/00/19/32/48/PDF/TheseRaufaste.pdf`
20. V. Labiausse, R. Höhler, S. Cohen-Addad, J. Rheol. **51**, 479 (2007).
21. M. Fortin, D. Côté, P.A. Tanguy, Comput. Methods Appl. Mech. Eng. **88**, 97 (1991).
22. N. Roquet, Ph.D. thesis, Université Joseph Fourier, Grenoble, France (2000) `http://ljk.imag.fr/membres/Pierre.Saramito/Nicolas-Roquet-these.pdf`